PAPER • OPEN ACCESS

Interpreting observations of ion cyclotron emission from large helical device plasmas with beam-injected ion populations

OPEN ACCESS
IOP Publishing | International Atomic Energy Agency
Nuclear Fusion
Nucl. Fusion **59** (2019) 096013 (16pp)
https://doi.org/10.1088/1741-4326/ab2ca2

Interpreting observations of ion cyclotron emission from large helical device plasmas with beam-injected ion populations

B.C.G. Reman[1], R.O. Dendy[1,2], T. Akiyama[3], S.C. Chapman[1], J.W.S. Cook[2], H. Igami[3], S. Inagaki[4], K. Saito[3] and G.S. Yun[5]

[1] Centre for Fusion, Space and Astrophysics, Department of Physics, Warwick University, Coventry CV4 7AL, United Kingdom of Great Britain and Northern Ireland
[2] CCFE, Culham Science Centre, Abingdon, Oxfordshire OX14 3DB, United Kingdom of Great Britain and Northern Ireland
[3] National Institute for Fusion Science, National Institutes of Natural Sciences, Toki, Gifu 509-5292, Japan
[4] Research Institute for Applied Mechanics, Kyushu University, Kasuga 816-8580, Japan
[5] Department of Physics, Pohang University of Science and Technology, Pohang, Gyeongbuk 37673, Korea, Republic of

E-mail: reman.bernard-charles-g@warwick.ac.uk

Received 28 January 2019, revised 20 May 2019
Accepted for publication 25 June 2019
Published 19 July 2019

Abstract

Ion cyclotron emission (ICE) is detected from all large toroidal magnetically confined fusion (MCF) plasmas. It is a form of spontaneous suprathermal radiation, whose spectral peak frequencies correspond to sequential cyclotron harmonics of energetic ion species, evaluated at the emission location. In ICE phenomenology, an important parameter is the value of the ratio of energetic ion velocity $v_{\mathrm{Energetic}}$ to the local Alfvén speed V_{A}. Here we focus on ICE measurements from heliotron-stellarator hydrogen plasmas, heated by energetic proton neutral beam injection (NBI) in the large helical device, for which $v_{\mathrm{Energetic}}/V_{\mathrm{A}}$ takes values both larger (super-Alfvénic) and smaller (sub-Alfvénic) than unity. The collective relaxation of the NBI proton population, together with the thermal plasma, is studied using a particle-in-cell (PIC) code. This evolves the Maxwell–Lorentz system of equations for hundreds of millions of kinetic gyro-orbit-resolved ions and fluid electrons, self-consistently with the electric and magnetic fields. For LHD-relevant parameter sets, the spatiotemporal Fourier transforms of the fields yield, in the nonlinear saturated regime, good computational proxies for the observed ICE spectra in both the super-Alfvénic and sub-Alfvénic regimes for NBI protons. At early times in the PIC treatment, the computed growth rates correspond to analytical linear growth rates of the magnetoacoustic cyclotron instability (MCI), which was previously identified to underlie ICE from tokamak plasmas. The spatially localised PIC treatment does not include toroidal magnetic field geometry, nor background gradients in plasma parameters. Its success in simulating ICE spectra from both tokamak and, here, heliotron-stellarator plasmas suggests that the plasma parameters and ion energetic distribution at the emission location largely determine the ICE phenomenology. This is important for the future exploitation of ICE as a diagnostic for energetic ion populations in MCF plasmas. The capability to span the super-

Alfvénic and sub-Alfvénic energetic ion regimes is a generic challenge in interpreting MCF plasma physics, and it is encouraging that this first principles computational treatment of ICE has now achieved this.

Keywords: Alfvén wave, ion cyclotron emission, magnetoacoustic cyclotron instability, large helical device, neutral beam injection, HPC, hybrid-PIC

(Some figures may appear in colour only in the online journal)

1. Introduction

Suprathermal ion cyclotron emission [1, 2] (ICE) is detected from all large toroidal magnetic confinement fusion (MCF) plasmas including the tokamaks TFR [3], PDX [4], JET [5], TFTR [6], JT-60U [7], ASDEX-U [8], KSTAR [9], DIII-D [10] and the stellarators LHD [11, 12] and W7-AS [13]. ICE is notable as the first collective radiative instability driven by confined fusion-born ions that was observed in deuterium–tritium (D–T) plasmas in JET and TFTR [14–17]. The frequency spectrum of ICE typically exhibits narrow peaks at values which can be identified with sequential local cyclotron harmonics of a distinct energetic ion population in a spatially localised emitting region. The numerical value of the inferred ion cyclotron frequency $\Omega_c = Z_i eB/m_i$, where Z_i is the ion charge and m_i its mass, then determines the local value of the magnetic field strength in the emitting region, and hence its radial location. Typically, but not invariably, this is at the outer mid-plane edge of the toroidal plasma; ICE from the core plasma has been reported recently from DIII-D [18] and from ASDEX Upgrade [19], and earlier from JT-60U [7]. This development suggests great potential for the exploitation of ICE as a diagnostic for energetic particles in ITER [20].

Measurements of ion cyclotron emission (ICE) spectra have been obtained from heliotron-stellarator plasmas in the large helical device (LHD), both with an ICRH antenna during NBI heated plasmas [11] and by magnetic probes [12] during toroidal Alfvén eigenmodes (TAE's) [21–24]. Related numerical studies can be found in [24]. In combination with other advanced diagnostics, notably for MHD activity, these ICE measurements from LHD, can yield fresh insights into the physics of energetic ions in magnetically confined fusion (MCF) plasmas. We attribute this ICE to a neutral beam injected (NBI) proton population at energies ≈40 keV in the outer midplane edge regions of hydrogen plasmas in LHD [11, 12], where the local electron temperature $T_e \approx 20$ eV to 150 eV, number density $n_e \approx 10^{19}$ m^{-3} and magnetic field strength $B \approx 0.5$ T. These spectra were measured with an ICRF heating antenna in receiver mode. Importantly, these spectra span plasma regimes where the ratio of the velocity of the energetic ions V_{NBI} to the local Alfvén speed V_{A} in the ICE-emitting region of the LHD edge plasma takes values that can be either smaller or larger than unity. The transition between super-Alfvénic and sub-Alfvénic energetic ion phenomenology is of fundamental interest in MCF plasma physics, see section 2 below. Here, in particular, we examine LHD plasmas 79126 and 79003 where $V_{\mathrm{NBI}}/V_{\mathrm{A}} = 0.872$ and 1.125, respectively, in the ICE-emitting region.

Our interpretation rests on first-principles numerical solutions of the Maxwell–Lorentz system of equations. We follow the full velocity-space trajectories, including gyromotion, of tens to hundreds of millions of fully kinetic energetic and thermal ions, together with all three vector components of the evolving electric and magnetic fields, with a massless neutralising electron fluid, using a fully nonlinear 1D3V PIC-hybrid particle-in-cell code [25]. The kinetic ions, fluid electrons, and fields are coupled self-consistently through the Lorentz force and Maxwell's equations in Darwin's approximation [26]. In this hybrid scheme [25], the Debye length does not need to be resolved. It therefore requires less computational resource than the full PIC scheme implemented in EPOCH [27], which retains electron kinetics, and is also used for contemporary theoretical studies of ICE [28–32]. We follow these simulations through the linear phase of an instability that we show is the magnetoacoustic cyclotron instability (MCI) [25, 29, 33–36], and then deeply into its nonlinear saturated phase. The Fourier transforms of the excited fields in these simulations yield frequency spectra that qualitatively match the observed ICE spectra from the LHD plasmas. These simulation results for heliotron-stellarator plasmas complement and confirm earlier interpretation of ICE driven by sub-Alfvénic NBI ions in TFTR tokamak plasmas [15, 37]. In general, ICE phenomenology in MCF plasmas has been found to reflect the plasma parameters and magnetic field strength in the emitting region, together with the velocity distribution of the driving energetic ion population. Important aspects of these two key features come together in the dimensionless parameter $v_{\mathrm{Energetic}}/V_{\mathrm{A}}$, which is the ratio of energetic ion velocity $v_{\mathrm{Energetic}}$ to the local Alfvén speed V_{A}.

2. The wider experimental context and motivation

In this work we focus on the role of the parameter $v_{\mathrm{Energetic}}/V_{\mathrm{A}}$ and, in particular, whether it exceeds, or is less than, unity. In general, one anticipates differences in how a particle interacts with the coherent oscillations that are supported by a continuous medium, depending on whether the particle is travelling faster or slower than the speed at which phase information can propagate in the medium. In a magnetised plasma, in the frequency range of interest to ICE, this speed is the Alfvén speed V_{A}. Even if no complete experimental or theoretical information related to this frequency and velocity range in

fusion plasmas is available, it would be necessary to investigate it when establishing the physics basis for the exploitation of ICE. However there exists, in addition, extensive evidence for the importance of the value of the ratio $v_{\text{Energetic}}/V_{\text{A}}$ compared to unity: in relation to the ICE detected from fusion-born alpha-particles in the only DT MCF plasmas thus far, in JET and TFTR during the 1990s; and in relation to the fundamental theory of the MCI.

The fusion-born alpha-particles responsible for the ICE observed throughout the duration of JET DT H-mode plasmas with high edge density were super-Alfvénic, see the sixteenth item in table 1 of [14]; whereas in TFTR supershot DT plasmas with strong central density peaking and low edge density, they were sub-Alfvénic, as shown in figure 6 of [15]. Apparently related to this, and shown in figure 7 of [15], alpha-particle ICE from TFTR DT plasmas arose only during the first 100 ms to 200 ms, in the early stage of the density ramp, notwithstanding the greater measured production rate for fusion alpha-particles at later times with higher density. Conversely, in TFTR plasmas with edge densities such that newly born alpha-particles were super-Alfvénic, the corresponding alpha-particle ICE spectrum persisted, see [15]. Evidently the value of $v_{\text{Energetic}}/V_{\text{A}}$ is central to the ICE phenomenology in the DT plasmas which, thus far, provide the most relevant signposts for ICE if it arises in ITER.

The earliest study [37] of ICE driven by NBI ions in TFTR DT plasmas reinforced the centrality of $v_{\text{Energetic}}/V_{\text{A}}$, bearing in mind also that NBI ICE was not detected from JET DT plasmas. For example, deuterium and tritium NBI ions were at $v_{\text{Energetic}}/V_{\text{A}} = 0.1$ in the plasma region where they excited ICE. The analytical MCI theory available at that time [34–36] was aligned to the JET super-Alfvénic alpha-particle regime, and could not immediately address the strongly sub-Alfvénic TFTR NBI regime; instead an interpretation was obtained based on a primarily electrostatic treatment [37].

The foregoing motivated the extension of the analytical theory of the MCI into the sub-Alfvénic regime, reported at length in [36], and exploited in [14] and in relation to both NBI ions and fusion-born ions in [16, 38]. By this stage, the linear analytical theory of the MCI had successfully exhausted its potential at the leading edge of ICE interpretation. Only from 2010 onwards was it possible to carry out first principles kinetic calculations using PIC codes, which carry the MCI self-consistently into its fully nonlinear regime [25, 30–32, 39]. The saturated power spectra emerging from these computations then provide theoretical counterparts to measured ICE spectra. Hitherto, with one exception, these treatments have addressed only the super-Alfvénic regime for fusion-born ions. The exception is the set of multiple PIC simulations [31, 32] of ICE driven by fusion-born protons under rapidly evolving edge plasma conditions in KSTAR. For local electron densities below $n_e \sim 1.05 \times 10^{19}$ m^{-3}, corresponding to the lower panels of figure 4 of [31], the perpendicular velocity of the protons is sub-Alfvénic.

It is therefore timely to address the standing issue of the impact on ICE of the value of the ratio $v_{\text{Energetic}}/V_{\text{A}}$ compared to unity, by using a combination of contemporary NBI ICE measurements and PIC computations. Here we exploit the fact that ICE from the outer midplane edge of LHD heliotron-stellarator plasmas is generated by NBI ions in both super-Alfvénic and sub-Alfvénic regimes. We use the hybrid PIC code of [25], as previously exploited along with the EPOCH PIC code [27] in [25, 30–32, 39], to simulate the collective relaxation of these NBI ion populations under LHD-relevant conditions.

To progress, several novel steps are necessary, which are reported in this paper. We carry out the first extensive set of 1D3V kinetic PIC-hybrid simulations of ICE in the sub-Alfvénic regime, where the minority NBI ion population has kinetic energy more than an order of magnitude lower than in previous simulations [25, 30–32, 39] relating to super-Alfvénic fusion-born ions in JET. These are also the first ICE simulations with wavevectors inclined more than one degree from perpendicular to the magnetic field direction. The analytical theory of the linear MCI which underlies ICE is well developed, and we are able to show that its predictions regarding initial growth rates in our fully nonlinear simulations are successful, for the first time in the sub-Alfvénic regime.

3. Introduction to ICE theory and interpretation

3.1. Analytical theory of the magnetoacoustic cyclotron instability

The magnetoacoustic cyclotron instability (MCI) [25, 29, 33, 34, 36, 37, 38] is the most likely emission mechanism to account for ICE generation. The theory of the MCI was first developed analytically [33–36], and then using large PIC numerical simulation from 2010 onwards [29, 30, 39]. At the plasma wave-wave resonant level of description, the MCI essentially involves the resonance of a fast Alfvén wave supported by the background plasma with negative-energy ion cyclotron harmonic waves (terminology described in the next paragraph) sustained by minority fast ions whose non-Maxwellian velocity distribution incorporates a population inversion. This is evident from the structure of the left-hand side of equation (28) of [34] for example. MCI theory was originally developed by [33] for purely perpendicular propagating waves satisfying $\omega \gg \Omega_i$, the background ion cyclotron frequency, including a ring beam distribution for fast ions. The theory was revisited and extended in [34] to lower frequencies for perpendicular propagation, and MCI growth rates were further obtained for energetic ion distributions in velocity space that have the form of both a spherical and an extended-spherical shell [35], in addition to monoenergetic ring beams [33, 40]. The interest in the ring beam-type distribution arose from the subset of fast ions thought to be responsible for generating ICE from DT plasmas in JET and, subsequently, TFTR. These ions, born in a very narrow range of pitch angles, undergo large drift orbit excursions from the core whose trajectories intersect the outer midplane edge. This leads to a local population inversion in velocity space, in the form of a thin cone shape which is limited by: the maximum energy of the α particles; their narrow range of pitch angles; and, at the lower bound, the strong decrease of radial excursion with decreasing energy (figure 15 of [14]).

The negative energy character of the ion cyclotron harmonic waves supported by the energetic ion population, alluded to in the preceding paragraph, is a key element—explicit or otherwise—in all theories of the MCI. Less importantly, the ion cyclotron harmonic waves supported by the bulk plasma also enter the left-hand-side of equation (28) of [34] and, if resonant, can change the order (quadratic to cubic) of the analytical expression for the growth rate in the linear limit. Neglecting this complication, when the linear MCI occurs, there is spontaneous growth in amplitude of both the fast Alfvén wave supported primarily by the bulk plasma, and the cyclotron harmonic wave supported by the non-Maxwellian alpha-particle population. This does not violate energy conservation because the latter wave is negative-energy: its excitation lowers the overall energy of the system which supports it. Negative-energy waves can only arise where there is a distinctly non-Maxwellian population, for example beam-type, in velocity space; for an account of this, see [41].

The analytical theory of the MCI was extended to include wave-particle cyclotron resonance in [34]. In this form, it was applied to the interpretation of ICE measurements from DT plasmas in JET and TFTR, including sub-Alfvénic regimes in [36, 37]. The MCI is also believed to play a central role in the excitation, by energetic ion populations in spherical tokamaks, of compressional Alfvén eigenmodes [42–45] (CAEs). CAEs can be viewed as a toroidal generalisation of the fast Alfvén wave (or of the magnetosonic wave) at frequencies comparable to, or lower than, Ω_{H}, the energetic ion cyclotron frequency. Hence this phenomenon may in some respects be a lower-frequency continuation of ICE phenomenology. Among the most sophisticated numerical approaches in this context is the HYM code [46], which represents the energetic ion population using a full-orbit delta-*f* approach, and the background plasma by single-fluid resistive MHD equations. The delta-*f* method [47] is a particle-in-cell approach for the solution of the perturbed velocity distribution function. With this method, only the deviation of the initial velocity distribution is treated in a PIC-fashion. This has the advantage to significantly reduce the noise in the simulations since only a subset of the velocity space is represented by means of macroparticles.

Finally, we recall that with the introduction of tritium into JET in 1991 [48], ICE was detected at successive cyclotron harmonics of α particles. The intensity of this ICE extended the linear correlation with the measured neutron flux [14] to over six decades of signal intensity across all classes of JET plasma. Also, a striking correlation was obtained between the maximum linear growth rates computed via the MCI linear analytical theory and the time evolution of the ICE amplitude averaged over six TFTR supershots, see figure 6 of [38]. This calculation was carried out using a drifting Maxwellian for the parallel distribution function of the fusion-born alphas and a ring-beam for the perpendicular velocity distribution function. In [49], additional conclusions are drawn. In particular, the aforementioned distribution function gives rise to a sublinear scaling of the linear analytical growth rates ($\propto\sqrt{n_\alpha/n_e}$) with increasing alpha density, in a regime where linear theory is not applicable, see figure 7 of [49]. This was taken to indicate that the linear scaling of ICE intensity with fusion alpha density in TFTR suggested that the relative alpha density at the emission location was smaller than 10^{-4}. The PIC simulations of ion cyclotron emission have mostly, so far, assumed ring beam distributions or drifting ring beams; this includes the present paper. Such ring beams were used as initial alpha particles velocity distribution of hybrid PIC simulations of the MCI relevant to JET ICE [25], which showed that the linear growth rates scaled sublinearly with the alpha particles density, in agreement with the relevant linear theory (equation (36) of [34]). These simulations further suggested that the spectral power of the nonlinearly saturated fields scaled linearly with the alpha density as observed experimentally in JET.

3.2. First principles numerical simulations of ICE

Direct numerical simulations of ICE scenarios were first reported in 2013 [29]. These used a particle-in-cell (PIC) [50–52] code [27] (see also section 5) to evolve the full orbit kinetics of millions of thermal ions and electrons, together with the self-consistent electric and magnetic fields, all governed by the Maxwell and Lorentz equations. The distribution of energetic ions in velocity space is initialised to reflect physics considerations relevant to the observations of ICE. PIC simulations motivated by ICE measurements from JET show [25, 29] that energetic minority ions relax, under Maxwell–Lorentz dynamics, in ways that replicate the linear MCI at early times and, at later times, produce power spectra capturing measured ICE features. Multiple simulations with different concentrations of energetic ions predict a linear scaling of spectral peak intensity that matches the observed linear scaling of ICE intensity with fusion reactivity [39] in JET. An ICE-related scenario relevant to α-channelling [53] has been proposed on the basis of PIC simulations [30]. It rests on a process that can arise when a radially inward propagating fast Alfvén wave, unstable against the MCI in the outer edge plasma, thereby extracts energy from a fast ion population and transfers it to the bulk plasma.

4. ICE measurements from NBI-heated LHD hydrogen plasmas

Highly resolved ICE signals were measured in LHD hydrogen plasmas using an ICRF antenna in receiver mode [11] during perpendicular neutral beam injection (NBI) of hydrogen ions. The large antenna loop area ($\approx$600 cm^2) enhances the quality of the data, which was recorded at a maximum sampling rate of 5GSas^{-1} and processed via fast Fourier transform, with a rectangular window of typical duration 100 μs. Examples of time profiles of heating with four proton NBI sources, together with ICE spectra, are shown in figures 1 and 2. These spectra obtained from LHD plasmas 79126 and 79003 are not discussed in 11 and 12, but share key similarities in that they all pertain to hydrogen plasmas heated by neutral beam injection: specifically, 40 keV perpendicular NBI giving rise to ICE, as presented in [11] and [12] and simulated in the present work. These ICE signals discussed in [11, 12] are detected shortly

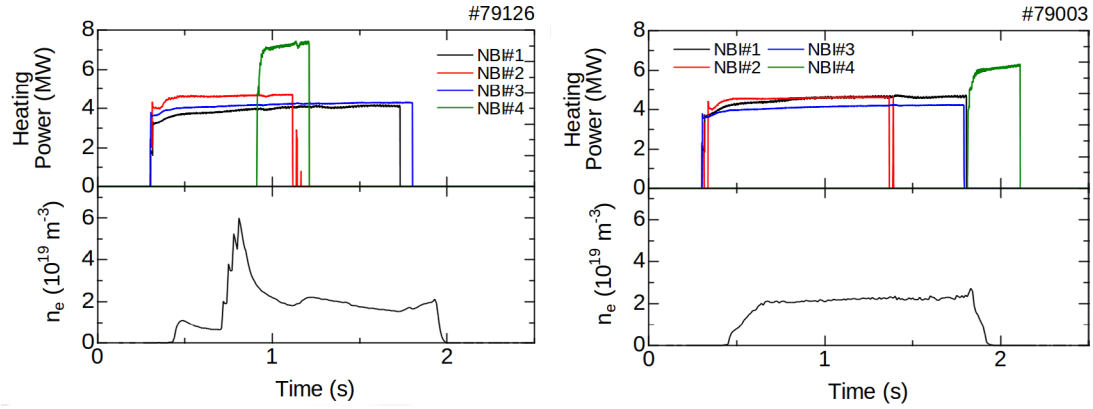

Figure 1. Time histories of NBI evolution (top panels) and line-integrated densities (bottom panels) in sub-Alfvénic LHD plasma 79126 (left) and in super-Alfvénic LHD plasma 79003 (right). In both cases, the ICE is concurrent with perpendicular NBI #4, at $t \approx 1.210$ s (left) and at $t \approx 1.817$ s (right).

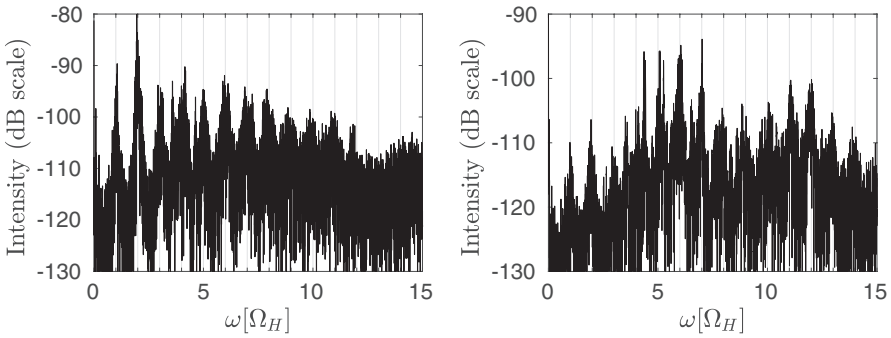

Figure 2. *B* field power spectrum for perpendicular 40 keV sub-Alfvénic (left) and for perpendicular 36.5 keV super-Alfvénic (right) NBI protons from LHD plasmas 79126 and 79003 respectively. The radiation originates at $R_{ax} = 4.62$ m corresponding to $\Omega_H = 6.75$ MHz (left) and at $R_{ax} = 4.65$ m corresponding to $\Omega_H = 3.67$ MHz (right), which we identify with the observed separation f_0 between successive spectral peaks, see figure 3. Up to measurement errors, the local plasma temperature $T_e \approx 150$ eV and density $n_e \approx 10^{19}$ m^{-3} for sub-Alfvénic LHD plasma 79126 (left) while the local plasma temperature $T_e \approx 25$ eV and density $n_e \approx 0.5 \times 10^{19}$ m^{-3} for super-Alfvénic LHD plasma 79003 (right).

after the turn-on of the perpendicular positive-ion based NB injector #4 by an antenna located close to it, at the outer mid-plane of LHD.

The fundamental ICE frequency f_0 is defined by the measured interval between successive spectral peaks, and also typically corresponds to the frequency of the first measured spectral peak. A linear relation was obtained between f_0 and the magnitude of the magnetic field on axis (at a major radius of 3.6 m) across several LHD plasmas, confirming the cyclotronic character of the detected signal. It follows that the location at which this ICE signal is generated in LHD lies along a magnetic field line on which the proton cyclotron frequency f_{cH} corresponds to the measured fundamental ICE frequency f_0, see figures 3 and 4 of [11]; this is found to be at both the LHD plasma inner and outer edge in the LHD magnetic configuration (see figure 3 of [11]). The observation of ICE from high density ($n_e > 5 \times 10^{20}$ m^{-3}) LHD plasmas, into which NBI cannot penetrate as far as the inner edge, further supports the interpretation that ICE originates from the outer region near the NBI #4 injection point. The ICE signal in the plasmas of [11] disappeared roughly 0.1ms after the turn-off of the perpendicular NBI (see figure 5 of [11]). This synchronization suggests that ICE is driven by the fast injected protons. Particle orbit calculations [11] for the relevant LHD plasma and magnetic field show that NBI protons are lost in a few tens of microseconds, consistent with the observed decay time of ICE.

5. Direct numerical simulation of LHD ICE using a kinetic PIC-hybrid code

In this paper, we will interpret the ICE spectra shown in figures 1 and 2, in terms of the collective relaxation of the NBI proton population in the LHD plasma edge. To that purpose, we first introduce the PIC-hybrid modelling approach. We then present the physical and computational parameters involved in the calculations. In particular, this study requires, as input, a representation of the distribution in velocity-space of the NBI protons which is based on the kinetic modelling of [54] that we briefly describe. We then move on to present our calculations results.

5.1. The PIC-hybrid approach

We use the one spatial dimension and three velocity space dimensions (1D3V) PIC-hybrid code [55, 56] approach

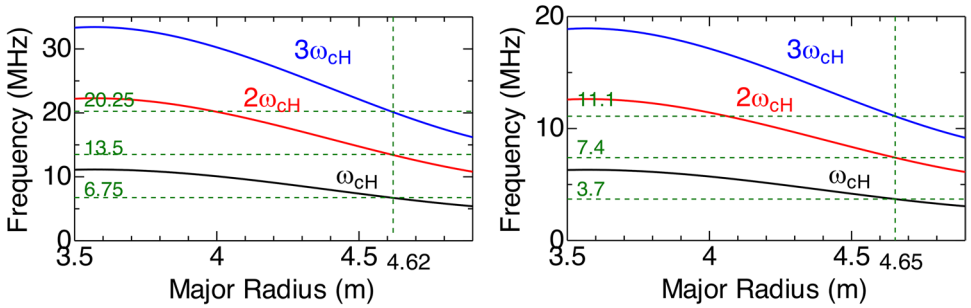

Figure 3. Dependence of the local value of the proton cyclotron harmonic frequencies on major radial position in LHD plasmas 79126 (left) and 79003 (right). The measured spectral peak separations f_0 in figure 2 are identified with the proton cyclotron frequencies $\Omega_H = 6.75$ MHz and $\Omega_H = 3.67$ MHz respectively. The corresponding magnetic fields have magnitude 0.46 T and 0.24 T. We infer that ICE is emitted at $R_{ax} = 4.62$ m (left) for LHD plasma 79126, and at $R_{ax} = 4.65$ m (right) for LHD plasma 79003.

implemented in [25]. This follows full gyro-orbit kinetics for ions in collisionless plasmas, where the energetic and thermal populations are represented by hundreds of thousands to hundreds of millions of macro-particles. These interact with each other, and with the self-consistent electric and magnetic fields, through the Lorentz force and Maxwell's equations. The code incorporates all three vector components of the electric and magnetic fields, and of each particle's velocity, and represents the electrons as a massless neutralising fluid. It self-consistently solves and iterates the Lorentz force equation for each particle together with Maxwell's equations in the Darwin approximation [20, 55] which neglects the displacement current and alleviates the needs to resolve light waves; it is fully nonlinear. The code resolves ion gyromotion, which is necessary to simulate phenomena such as ICE where key physical length scales and time scales are of the order of the ion gyro-radius (and ion skin depth) and ion cyclotron frequency. In particular, the code captures the full spatial and gyrophase dynamics of resonant particle-field interactions close to the ion cyclotron frequency and its harmonics. We assume quasineutrality:

$$\sum_{l=1}^{N} Z_l n_l = n_e \tag{1}$$

with n_e the number density of electrons and n_l, Z_l the number density and electric charge of each ion species l. We also have

$$\nabla \cdot \mathbf{B} = 0 \Rightarrow B_x = 0 \tag{2}$$

where x denotes distance along the 1D slab geometry spatial domain of our code. We solve for $\mathbf{B}$ using Faraday's law

$$\frac{\partial \mathbf{B}}{\partial t} = -\nabla \times \mathbf{E} \tag{3}$$

while Ampère's law in the Darwin approximation [26] combines with the massless electron momentum equation to give the generalized Ohm's law [57],

$$\mathbf{E} = \frac{1}{\mu_0 e n_e} (\nabla \times \mathbf{B}) \times \mathbf{B} - \mathbf{V}_i \times \mathbf{B} - \frac{\nabla p_e}{e n_e}. \tag{4}$$

Here the charge-weighted mean ion velocity $\mathbf{V}_i$ is defined by

$$\mathbf{V}_i = \frac{\sum_{l=1}^{N} Z_l n_l \mathbf{u}_l}{\sum_{l=1}^{N} Z_l n_l} \tag{5}$$

where $\mathbf{u}_l$ denotes the bulk ion velocity of species l. We assume an isothermal pressure law, $p_e = n_e k_B T_e$, with T_e the electron temperature. A quiet start [50, 58] is used to launch the majority thermal ions in phase space, so as to reduce the noise in our simulations. The code makes use of periodic boundary conditions. This level of approximation is known to sustain fluid waves such as the fast Alfvén and whistler waves, as well as kinetic waves such as electrostatic Bernstein and ion cyclotron modes.

5.2. Physical and computational parameter sets

The NBI protons are sub (super)-Alfvénic in the emitting region of LHD hydrogen plasmas 79126 (79003), whose measured ICE spectra are shown in figure 2 and again in figure 7. Their initial energies are 40 keV (36.5 keV), corresponding to a proton perpendicular injection velocity $v_{NBI} = 2.77 \times 10^6$ ms^{-1} (2.64×10^6 ms^{-1}). To approximately represent LHD edge plasma conditions in the simulations reported here, the thermal electrons and ions both have a temperature of 0.150 (0.025) keV, the electron density is 10^{19} m^{-3} (5×10^{18} m^{-3}), and the background magnetic field has strength $B_0 = 0.46$ (0.24) T. The local Alfvén speed V_A is therefore 3.17 (2.35) $\times 10^6$ ms^{-1}, hence the NBI protons are sub (super)-Alfvénic with $v_{NBI}/V_A \approx 0.870$ (1.125). In our simulations, the 40 (36.5) keV NBI proton population is taken to have particle concentration $\xi = 5 \times 10^{-4}$ (7.5×10^{-4}) relative to the thermal ions. Concentration $\xi = n_{NBI}/n_e$ is chosen at a level that gives rise to saturation of the MCI within the simulation run time.

Denoting the spatial component of the 1D3V simulation domain by $\hat{\mathbf{x}}$, the wavevector $\mathbf{k} = k\hat{\mathbf{x}}$; in our simulations, the angle between $\mathbf{B}_0$ and $\mathbf{k}$ is 89.5° or 85.0°. For 89.5° propagation angle, there are 22080 (10560) computational cells and 4000 (500) macroparticles per cell. The cell size is 0.61 (1.06) times the thermal ion Larmor radius $r_L = 0.0031$ (0.0025) m; for neutral beam ions $r_{L,NBI} = 0.063$ (0.115) m. This implies that the simulations resolve 1.35 (1.12) $\times 10^4$ background proton gyroradii or 670 (240) NBI fast proton gyroradii. Once the cell size has been chosen for each instance (usually of the order of the electron skin depth), the different number of cells used leads to grids that resolve the same number of background plasma gyro radii.

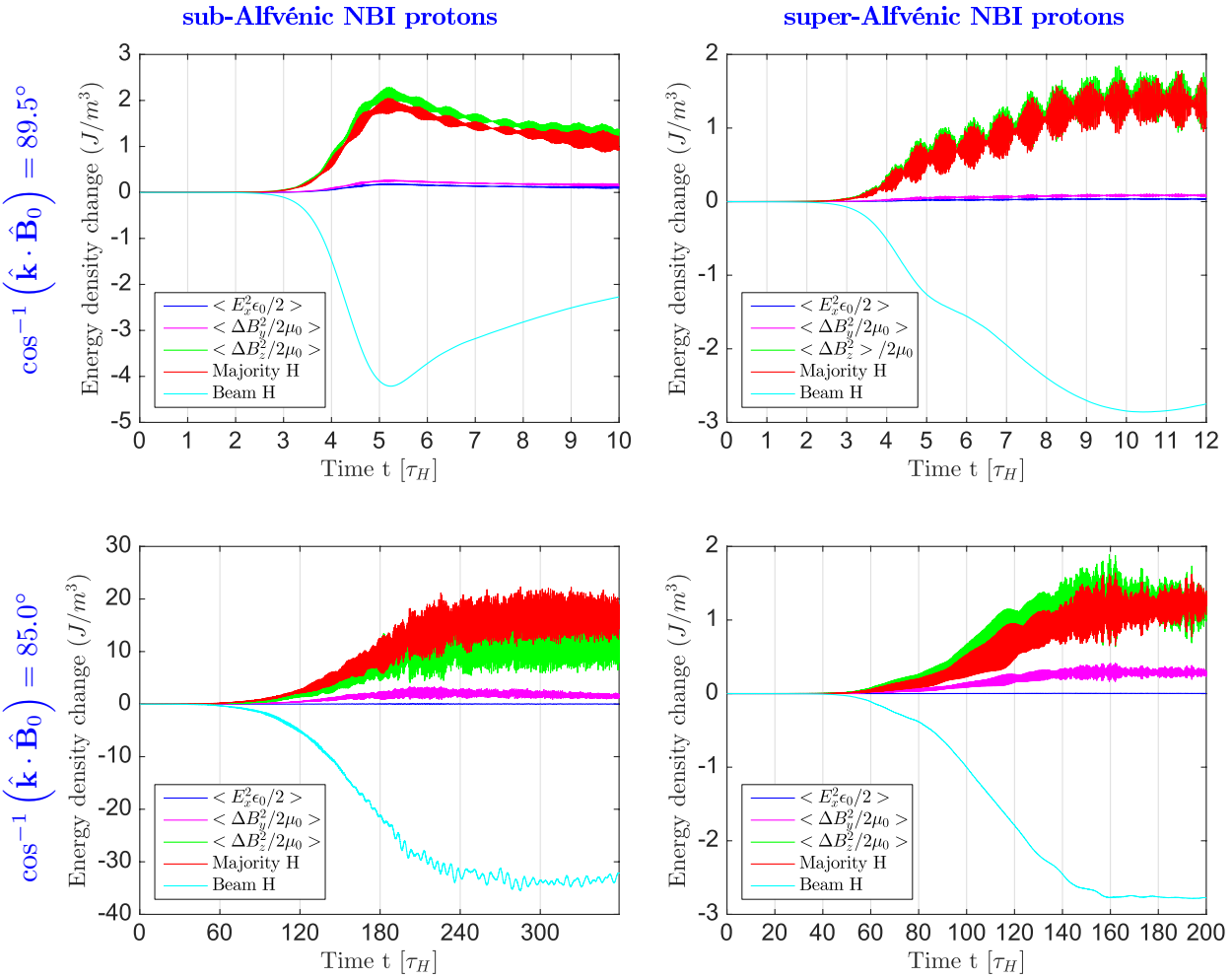

Figure 4. Time evolution (horizontal axis, in units of proton gyroperiods τ_H) of the energy density change of different field components and particle populations in four PIC-hybrid simulations. Left panels are for LHD hydrogen plasma 79126 with sub-Alfvénic 40 keV NBI protons, for which $v_{\mathrm{NBI}}/V_{\mathrm{A}} = 0.872$. Right panels are for LHD hydrogen plasma 79003 with super-Alfvénic 36.5 keV NBI protons for which $v_{\mathrm{NBI}}/V_{\mathrm{A}} = 1.125$. Top panels are for propagation angle of $\mathbf{k}$ with respect to $\mathbf{B}_0$ of 89.5°. Bottom panels are for propagation angle 85°. Concentration $\xi = n_{\mathrm{NBI}}/n_e$ is chosen at a level that gives rise to saturation of the MCI within the simulation run time: $\xi = 5 \times 10^{-4}$ at top left and bottom right; $\xi = 7.5 \times 10^{-4}$ at top right; and $\xi = 5 \times 10^{-3}$ at bottom left. Red trace: bulk protons. Cyan: NBI protons. Green z-component and magenta y-component of the fluctuating part of the magnetic field. Dark blue: x-component of the electric field. The excitation of the y-component of the magnetic field is due to the NBI protons that have a velocity component along the z direction, while $\mathbf{k}$ is along the 1D simulation domain ($\hat{\mathbf{x}}$ direction). The NBI protons typically release 10%–15% of their energy to the background protons and to the electric and magnetic fields. Saturation of the instability occurs after ≈1 μs to 100 μs. This time is similar to the time window used to compute the LHD power spectra (see figure 2 of [11]).

The increased number of particles per cell in the sub-Alfvénic calculations reduces the noise in the simulations, and facilitates the calculation of the growth rates presented in Section 6. The simulations at 85° between ω and $\mathbf{k}$ use fewer particles per cell and a larger grid length, which enables us to run the simulations for longer as shown in figure 4.

The time step is $0.00025\ \ (0.0001) \times \tau_{\mathrm{H}}$, where $\tau_{\mathrm{H}} = 0.143\mu s\ \ (\tau_{\mathrm{H}} = 0.273\mu s)$ is the proton gyroperiod in each simulation. Cyclotron motion is thus highly resolved, in space and time, for the energetic ions whose cyclotron resonant collective relaxation underlies the observed ICE signals. The simulations run for 10–360τ_{H}; this is determined by the time taken for the instability driven by the NBI ions to saturate, which for a given set of plasma parameters depends on ξ and on propagation angle. Physical and computational parameters for our simulations are summarized in tables 1 and 2 respectively. When necessary, subcycling for the electric and magnetic fields is used to satisfy the Courant–Friedrichs–Lewy (CFL) condition for the Alfvén wave [47], which states that to ensure the simulations are stable, $v_{\mathrm{max}} \times \Delta t < \Delta x$, v_{max} being the maximum velocity in the calculation. This means for example that a macroparticle can cross at most one cell over a timestep Δt. In our simulations, energy is conserved to within 0.2%.

5.3. Distribution in velocity-space of the NBI protons

Kinetic modelling [54] has previously been used to obtain the steady-state distribution function of NBI fast ions in stellarators, for both TJ-II and LHD. The LHD case focused on hydrogen plasmas heated by 40 keV perpendicular NBI, relevant to our study. The orbit code ISDEP (integrator of

Table 1. Summary of the physical parameters used in the PIC-hybrid ICE simulations for LHD plasmas 79126 and 79003. The quantity λ_D corresponds to the Debye length while λ_e and λ_H are the electron and proton skin depth respectively. The thermal plasma Larmor radii are expressed by r_L and the plasma beta by β while Ω_H and ω_H are the proton cyclotron and plasma frequencies respectively.

Quantity	Plasma 79126	Plasma 79003
Regime	sub-Alfvénic	super-Alfvénic
NBI injection energy	40 keV	36.5 keV
v_{NBI}/V_A	0.870	1.125
$T_e = T_H$	150 eV	25 eV
n_e	$1.0 \times 10^{19}\mathrm{m}^{-3}$	$0.5 \times 10^{19}\mathrm{m}^{-3}$
B_0	0.46 T	0.24 T
λ_D	2.35×10^{-5} m	1.35×10^{-5} m
λ_e	0.0017 m	0.0024 m
λ_H	0.0720 m	0.1019 m
r_L	0.0031 m	0.0025 m
β	0.19×10^{-4}	5.78×10^{-4}
ω_H/Ω_H	94.46	127.58

stochastic differential equations for plasmas) [54] is a Monte Carlo orbit-following code which solves the Fokker–Planck equation in 5D phase space, namely: (x, y, z, v^2, λ). The three spatial coordinates (x, y, z) are the guiding centre position, v^2 is a normalised kinetic energy, and $\lambda = \mathbf{v}\cdot\mathbf{B}/vB$ is a pitch angle. ISDEP includes collisions of fast ions with background ions and electrons, and treats re-entering particles. The initial NBI ion distribution function is calculated with HFREYA [59] which simulates the evolution of fast neutral particles by modelling their propagation, charge exchange and ionization processes. The resulting distribution in [54]'s work, which is relevant to perpendicular NBI in LHD, presents distinct features. Among them, the velocity distribution in pitch angles λ displays a peak near zero. The calculated velocity distribution function presents a ∼34 keV NB component which is close to the 36.5 keV super-Alfvénic initial fast proton population which, as we shall show, drives the ICE. The distribution is localized toroidally and the related density of fast neutrals increases with ρ, the dimensionless plasma radius defined in terms of toroidal flux surfaces. This NBI proton population is thus expected to arise close to NBI # 4, and therefore close to the ICRF receiver antenna. We shall therefore incorporate this form of minority energetic proton population in our first principles modelling of ICE in LHD.

The former motivates the initialisation of the NBI protons in velocity-space by means of a ring-beam velocity distribution function

$$f_{NBI}\left(v_\parallel, v_\perp\right) = \frac{1}{2\pi v_{NBI}}\delta(v_\parallel)\delta\left(v_\perp - v_{NBI}\right) \qquad (6)$$

and the NBI protons are initially uniformly and randomly distributed in gyro-angle. The orientation of the velocity of each NBI proton is thus perpendicular to the background magnetic field, in order to reflect the perpendicular orientation of the relevant NBI in LHD. The inclusion of this NBI ion population in our 1D3V simulations effectively defines the spatial location to which these simulations apply: that is, the location, near the NBI injection point at the outer midplane edge of LHD, where this NBI ion population is present.

5.4. Results of PIC-hybrid simulations

Figure 4 plots the time evolution, in our simulations, of the change in energy density of the electric and magnetic fields, and of the change in the kinetic energy density of the bulk proton and NBI proton populations. The four panels of figure 4 are for sub-Alfvénic (left) and super-Alfvénic (right) NBI protons, and for propagation angles θ of $\mathbf{k}$ with respect to $\mathbf{B}_0$ of 89.5° (top) and 85° (bottom). It is evident that the time taken for the NBI fast protons, which are not replenished, to relax, and for the instability which we identify below with the MCI to unfold, saturates on time scales of between $10\tau_H$ to $360\tau_H$. This corresponds to a few microseconds to a few 100 microseconds. The relative NBI proton concentration $\xi = n_{NBI}/n_e$ is chosen small enough to observe the unfolding of the MCI, yet not too small to reach saturation in a tractable computing time and for the ICE power to remain above the noise level. For this reason, the beam density is an order of magnitude higher ($\xi = 0.0050$) in the 79126 sub-Alfvénic LHD plasma simulation with propagation angle 85° compared with the other 3 simulations. The energy released at saturation by this 40 keV NBI proton population is one order of magnitude higher as a result, as can be observed from the bottom left panel of figure 4. More generally, the collisionless relaxation of the NBI protons under the MCI is slower at a propagation angle of 85.0° between the wavevector $\mathbf{k}$ and the background magnetic field $\mathbf{B}_0$ (bottom panels of figure 4) than it is at a propagation angle of 89.5° (top panels of figure 4). The growth rates are weaker for $\cos^{-1}\left(\hat{\mathbf{k}}\cdot\hat{\mathbf{B}}_0\right) = 85.0°$ than they are for $\cos^{-1}\left(\hat{\mathbf{k}}\cdot\hat{\mathbf{B}}_0\right) = 89.5°$. In all the results presented, the NBI protons have no initial velocity along the background magnetic field, for both propagation angles.

Spatio-temporal Fourier transforms of the excited fields are shown in figure 5, where the four panels correspond to the cases in figure 4. The simulated power spectra shown in figure 6 correspond again to the four panels in figures 4 and 5. These spectra, including also those in the bottom panels of figure 7, are constructed from figure 5 as follows: we compute the spatio-temporal fast Fourier transform (FFT) of the z-component of the fluctuating part of the magnetic field, δB_z, (figure 5), and then sum over wavenumbers between $k = 0$ and $k = 25\Omega_H/V_A$.

All the simulated spectra in figure 6 show strong excitation at multiple successive proton cyclotron harmonics; and the ICE signal in the simulations is a hundred to a thousand times more intense than the thermal noise. Decreasing the angle between k and B_0 shows preferential excitation at lower harmonics, as well as longer timescales for mode excitations, see figures 4 and 5. Since the power spectra at the bottom panels of figure 6 are averaged over a longer time duration (in particular compared to the proton gyroperiod), high spectral resolution is achieved that translates into the thick curves. The similar intensities on the top right and bottom right panels are due to comparable NBI proton densities. Conversely,

Table 2. Summary of the computational parameters used in the PIC-hybrid ICE simulations for LHD plasmas 79126 and 79003. The cell size Δx is greater or equal to λ_e in all simulations.

Quantity	Plasma 79126		Plasma 79003	
Regime	sub-Alfvénic		super-Alfvénic	
$\cos^{-1}\left(\hat{\mathbf{k}}\cdot\hat{\mathbf{B}}_0\right)$	89.5°	85.0°	89.5°	85.0°
Simulation duration	$[6, 20]\times\tau_H$	$360\times\tau_H$	$[12, 25]\times\tau_H$	$200\times\tau_H$
Number of grid cells	22080	1380	10560	2640
Number of part. per cell	4000	500	500	500
Δx	0.0019 m	0.0038 m	0.0026 m	0.0054 m
Length of simul. domain	$670\times r_{NBI}$	$84\times r_{NBI}$	$240\times r_{NBI}$	$125\times r_{NBI}$
	$13500\times r_L$	$1690\times r_L$	$11175\times r_L$	$5810\times r_L$
$\xi = n_{NBI}/n_e$	$[0.10, 0.60]\times10^{-3}$	5.0×10^{-3}	$[0.10, 1.90]\times10^{-3}$	0.5×10^{-3}

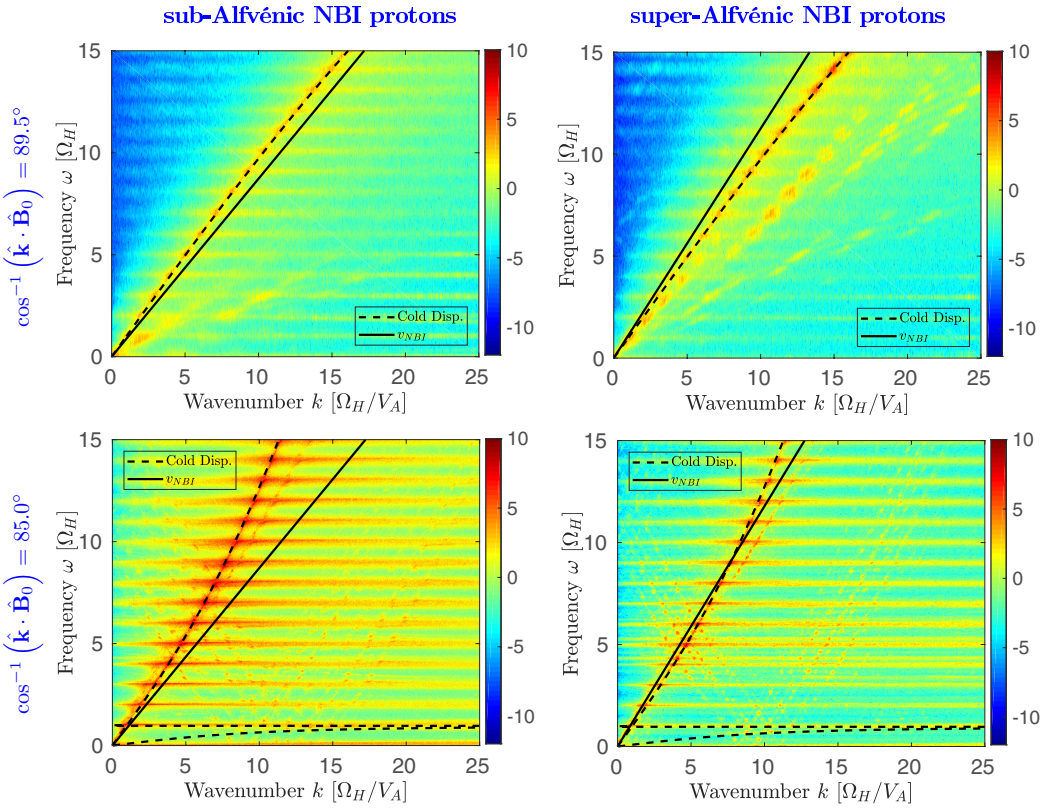

Figure 5. Spatio-temporal Fourier transform of the z-component of the fluctuating part of the magnetic field, δB_z, in the four PIC simulations whose energy evolution is shown in the corresponding panels of figure 4. The transform is calculated across the spatial domain and averaged over the simulation duration; magnitude is plotted on a $\log_{10}$ colour scale. The left and right pairs of panels correspond to simulations that have different values of NBI proton injection speed v_{NBI} compared to the Alfvén speed V_A, in the LHD plasma near the NBI injection point: (left) $v_{NBI}/V_A = 0.870$, (right) $v_{NBI}/V_A = 1.125$. Bright spots at sequential proton cyclotron harmonics along the fast-Alfvén branch result from the MCI, driven by NBI protons, for waves propagating in the $\hat{\mathbf{x}}$ direction, almost perpendicular to the background magnetic field. The cold plasma dispersion relation for the fast Alfvén wave, whose tangent at the origin satisfies $\omega = kV_A$, is shown by the dark dashed lines. The extension of the Alfvén wave below the proton cyclotron frequency arises from the finite parallel wavevector component on the bottom panels. The line $\omega = kv_{NBI}$ is shown by the dark trace, and lies above (or below) $\omega = kV_A$ in the super-Alfvénic (or sub-Alfvénic) NBI regimes. The wedge in $(\omega, \mathbf{k})$ space defined by these two lines approximately delineates the region of $(\omega, \mathbf{k})$ space where waves can in principle resonate with NBI protons. These plots show that, in our computations, excitation occurs for modes on the fast Alfvén branch and preferentially close to $\omega = kv_{NBI}$.

the proton beams densities differ by an order of magnitude on the top left and bottom left panels to saturate the MCI in a tractable computing time, whence the different intensities. The strong spike at $\omega = 0$ in figure 6 (top left) could be due to a numerical artifact during the post processing. This spike could also result from three-wave interaction between oppositely propagating waves such that $\omega_1 + \omega_2 = 0$ and $k_1 + k_2 = 0$. In the PIC-hybrid computations, the simulated emission is most strongly driven for propagation angles that are close to perpendicular to the magnetic field, for which the MCI is most unstable and saturates quickly as seen from the simulations at 89.5°.

Figure 7 shows good qualitative agreement between the spectra generated by relaxation of the NBI ion population in

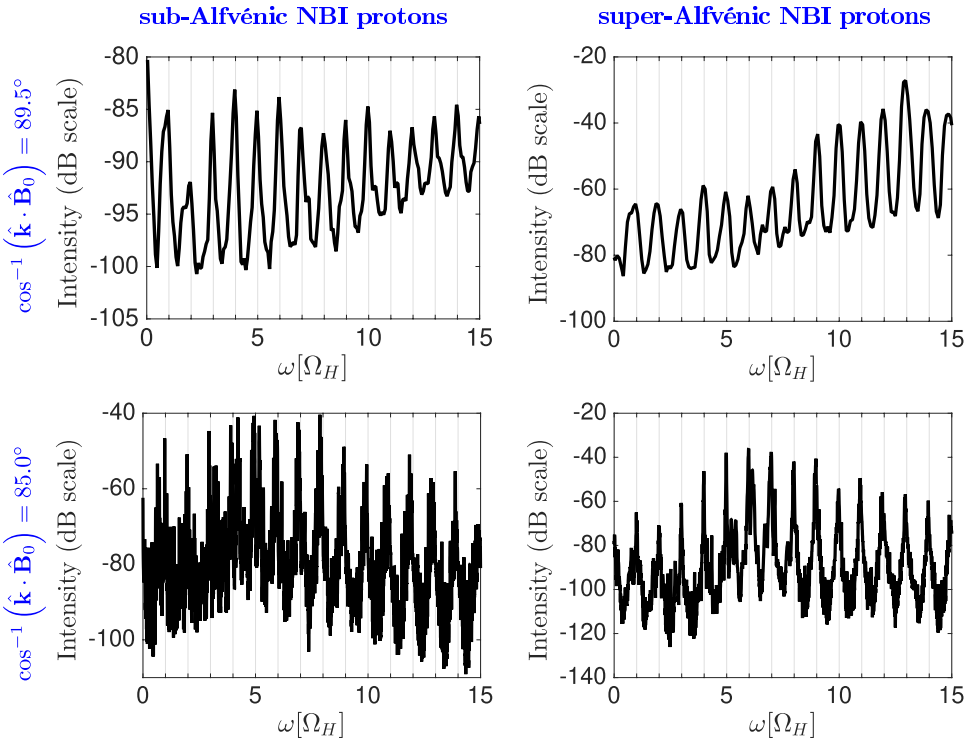

Figure 6. Power spectra $\delta B_z^2/B_0^2$ of the fluctuating z-component of the magnetic field in the four PIC-hybrid simulations whose energy evolution and spatiotemporal Fourier transforms are shown in the corresponding panels of figures 4 and 5 respectively. Power spectra are obtained using different orientations of the background magnetic field with respect to the 1D3V simulation, which defines the direction of **k**. Power spectra are obtained by taking the spatio-temporal Fourier transform of $\delta B_z(t) = B_z(t) - B_{0,z}$, averaged over the simulation duration and summed between $k = 0$ and $k = 25\Omega_{\rm H}/V_{\rm A}$. Peaks at multiple successive proton cyclotron harmonics are captured.

our first principles Maxwell–Lorentz computations with the 1D3V PIC-hybrid code, and the observed ICE spectra from LHD shown in figure 2, in both the sub-Alfvénic and super-Alfvénic NBI regimes in LHD. The ICE signals from LHD studied here were obtained in the same way as the early JET ICE measurements [5, 14], that is, using an ICRH antenna in receiver mode. The antenna has broad directionality, and in consequence can receive radiation across a wide range of incident angles. This is the reason for considering the emission at an angle of 85° whose corresponding simulated spectra are also shown at the bottom of figure 7. They show that ICE is still emitted away from pure perpendicular propagation under LHD edge plasma conditions and suggest the robustness of the MCI to drive ICE. In particular we infer that simulations at intermediate angles would generate ICE as well. Although the antenna cannot distinguish between incoming waves with a propagation angle of 89.5° and 85° separately, these would be summed together over the considered range of angles in forming the observed ICE spectrum. Here we compare the measured ICE spectra with our simulated spectra at 85°, which share a similar qualitative rise and then fall in the distribution of power across successive cyclotron harmonic peaks. At 89.5°, there is a monotonic increase of the power with harmonic number for the range of frequencies considered.

In figure 8, we plot the time evolution of the intensity of the spatial FFT of the magnetic field $\delta B_z^2/B_0^2$. There is a one-to-one mapping between the excited k-values and the cyclotron harmonics $\ell\Omega_{\rm H}$, inferred from the dispersion relation of the fast Alfvén wave using information in figure 5. Thus by plotting the time evolution of the distribution of energy across wavenumbers, as in Figure 8, we can identify the time sequence in which specific cyclotron harmonics in the simulated ICE spectrum are excited. A notable feature of figure 8 is the late excitation of the spectral peak at the fundamental cyclotron frequency of the protons in the nonlinear phase. This is of interest because, across multiple simulations, the fundamental cyclotron frequency is often the most strongly linearly stable against the MCI. The observational counterpart of this was noted early on, for example the early experimental comparison of ICE intensity spanning different levels of fusion reactivity in JET plasmas, figure 5 of [14], compares measured intensity at the second harmonic rather than the fundamental. In many simulations, ICE at the fundamental cyclotron frequency is driven by nonlinear beating between pairs of neighbouring higher harmonics that are linearly unstable. Examples include figure 1 of [25] for the MCI linear and nonlinear stability aspect, and figures 3 and 4 of [32] for nonlinear beating between neighbouring cyclotron harmonics in experimental ICE data and PIC simulation output respectively.

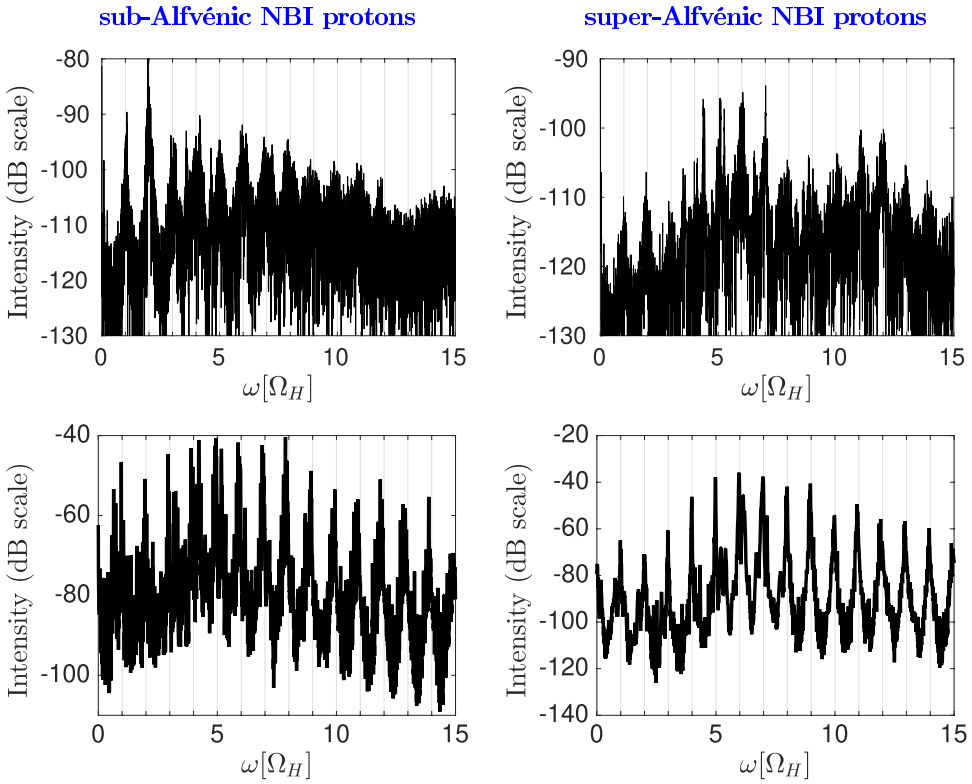

Figure 7. Comparison of measured and simulated ICE spectra, plotted on dB scales. Top panels: measured LHD ICE power spectra during sub-Alfvénic (left) and super-Alfvénic (right) perpendicular proton NBI, reproducing figure 2. Bottom panels: power spectra of $\delta B_z^2/B_0^2$ obtained from our PIC-hybrid simulations for parameters corresponding to LHD plasmas 79126 (left) and 79003 (right), see table 1, reproducing the bottom two panels of figure 6.

6. Identification of the excitation process in the PIC-hybrid simulations for NBI proton driven ICE in LHD plasmas

The frequencies of the modes excited by ICE in our simulations typically range from $\omega \approx 5\Omega_{\rm H}$ to $\approx 45\Omega_{\rm H}$. We focus primarily on modes up to $\omega \approx 15\Omega_{\rm H}$, marginally stable and unstable, to be in line with the upper frequency limit of the experimental measurements. These modes are electromagnetic and lie on the fast Alfvén branch, so that ω and k are related by $\omega \approx V_{\rm A}k$, where $V_{\rm A}$ is the Alfvén speed. In all the calculations that follow, we used the numerical dispersion relation to map k to ω; this relation satisfies the cold plasma dispersion of [60] and is necessary when ω starts to deviate from $kV_{\rm A}$. In our simulations, we consider waves propagating nearly perpendicular to the local background magnetic field. Such waves can leave an MCF plasma, propagating radially, and be detected beyond it. The simulation outputs encapsulated in figure 8 enable us to infer the rate at which the energy in a given cyclotron harmonic spectral peak grows over time. It is particularly helpful to calculate this during the early phase of growth, because this enables quantitative comparison with counterpart linear growth rates obtained from analytical theory. We denote the early phase growth rate inferred from the simulations at the ℓth harmonic by γ_ℓ. A primary objective is to quantify the scaling of γ_ℓ with NBI proton number density. This we shall compare with the corresponding scaling of analytical linear growth rate for the MCI, $\gamma_{\rm lin}(\ell)$, defined [14] by equations 7 and 8 below. Equation 9 shows that $\gamma_{\rm lin} \sim \xi^{1/2}$; hence figures 9 and 10 compare early phase simulation outputs with linear theory by plotting γ_ℓ versus $\xi^{1/2}$ for multiple simulations at a propagation angle of 89.5°, focusing on $\ell = 11$ and $\ell = 12$ for sub-Alfvénic NBI LHD plasma 79126 and super-Alfvénic NBI LHD plasma 79003 respectively. These harmonics are associated with the smallest error bars in our analysis. The agreement shown is good; this further confirms the role of the MCI in our simulations and, by extension, the LHD experiments.

Figures 9 and 10 are obtained as follows. The Alfvén dispersion relation provides a one-to-one mapping between the excited ω modes and the excited k modes. In addition, our simulations use an initially uniform density for both the NBI protons and the background plasma, and the domain has periodic boundary conditions. This means there is neither loss of information, nor need for windowing, when taking spatial Fourier transforms of the electric and magnetic fields. We may therefore compute the growth rates of k-modes by taking the spatial Fourier transform of $B_z(x,t)$, which we perform for a propagation angle of 89.5°, leading to $B_z(k,t)$ as shown on the top panels in figure 8. One selects an ω-mode at $\omega = \ell\Omega_{\rm H}, 5 \leqslant \ell \leqslant 15$, to which a unique k-mode, $k = k_{\ell\Omega_{\rm H}}$ is associated through the dispersion relation as in figure 5. The time evolution of $B_z\left(k_{\ell\Omega_{\rm H}}, t\right)$ is then plotted and best fits are constructed to extract the empirical growth rate γ_ℓ of this mode, as described below. This approach is convenient because it does not require transformations from

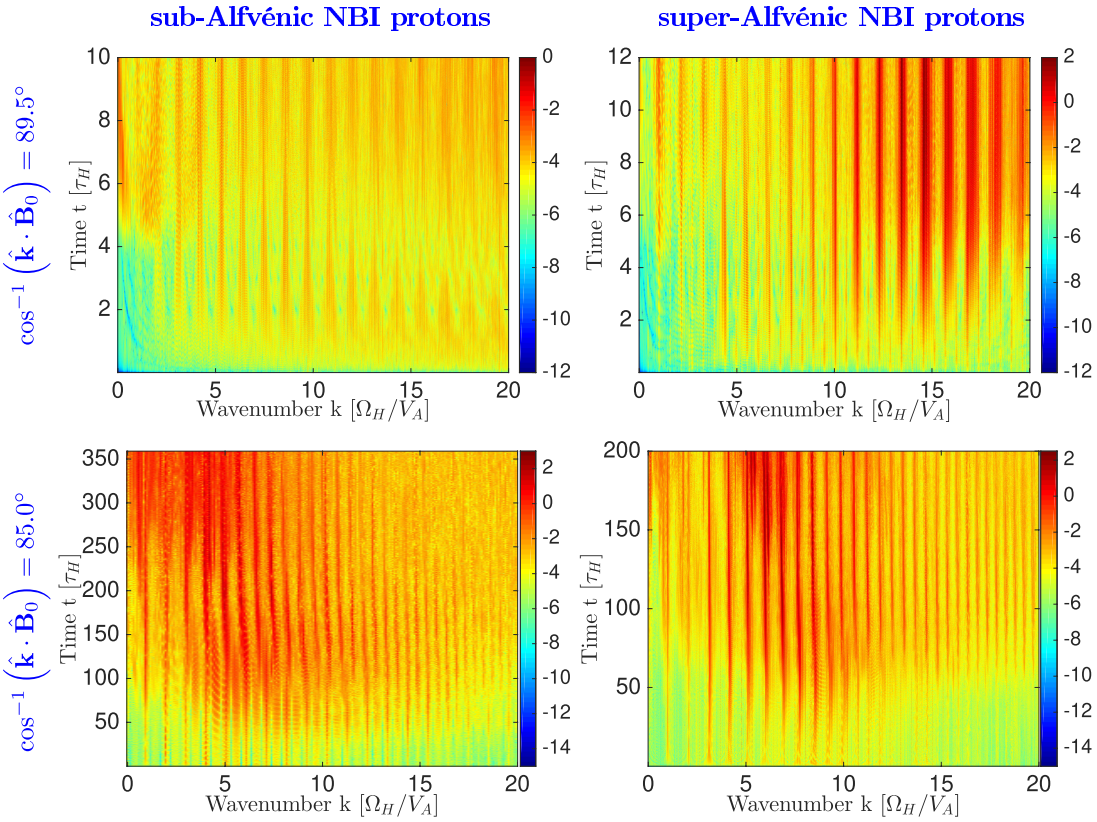

Figure 8. Time evolution (vertical axis, in units of proton gyroperiods τ_H) of the spatial Fourier transform of the z-component of the fluctuating magnetic field δB_z in the four PIC simulations whose energy evolution, spatiotemporal Fourier transforms, and ICE spectra are shown in the corresponding panels of figures 4–6 respectively. In each panel, the vertical time axis is identical to the corresponding horizontal time axis in figure 4. Magnitude is plotted on a log 10 colour scale. Wavenumbers are normalized to the proton skin depth Ω_H/V_A. The vertical bands correspond to the most strongly excited wavenumbers, which can be mapped to successive proton cyclotron harmonics using information in Fig 5. The modes excited earliest in the simulations are the most strongly linearly unstable ones, starting at cyclotron harmonic $\ell = 5$, approximately.

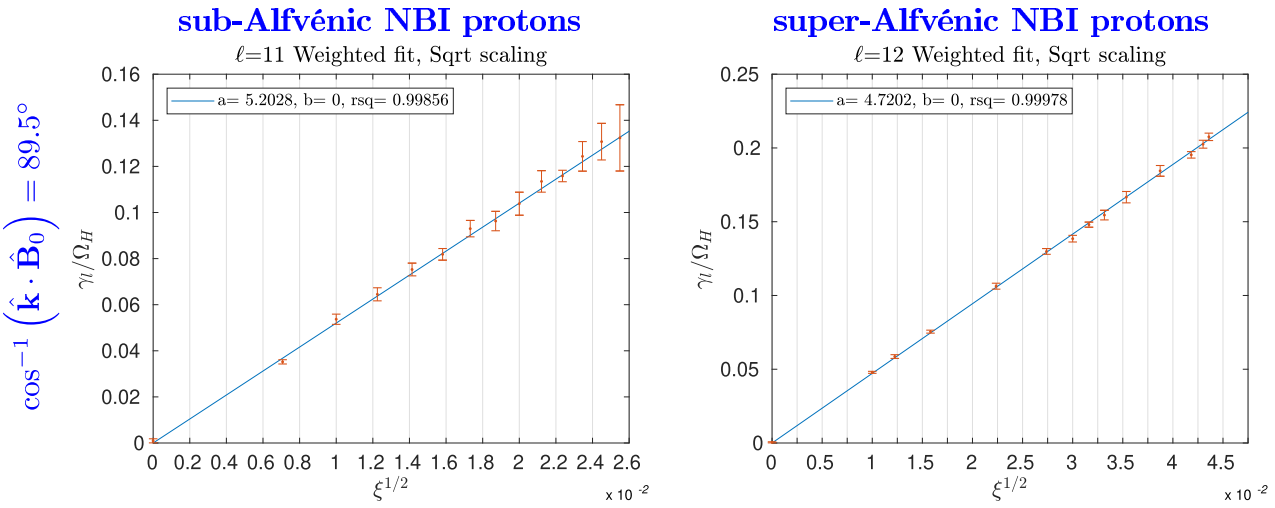

Figure 9. Linear fit of early phase growth rate γ_ℓ inferred from the simulations at an angle of 89.5°, normalized to Ω_H, against the square root of $\xi = n_{NBI}/n_e$, subject to the constraint that for a zero density beam, the line should intersect the origin. It is evident that the ICE growth rate γ_ℓ/Ω_H scales as $\sqrt{\xi}$. Left panel is for cyclotron harmonic mode $\ell = 11$ of the excited wave in the ICE emitting region of LHD plasma 79126 with locally sub-Alfvénic 40 keV NBI protons, and each point is for a value of ξ between 0.5×10^{-4} and 7.5×10^{-4}. Right panel is for cyclotron harmonic mode $\ell = 12$ of the excited wave in the ICE emitting region of LHD plasma 79003 with locally super-Alfvénic 36.5 keV NBI protons, and the values of ξ are between 1.0×10^{-4} and 2.0×10^{-3}. Note that contrary to table 1 and to figure 10, the x-axis is expressed in terms of $\sqrt{\xi}$ and not in terms of ξ.

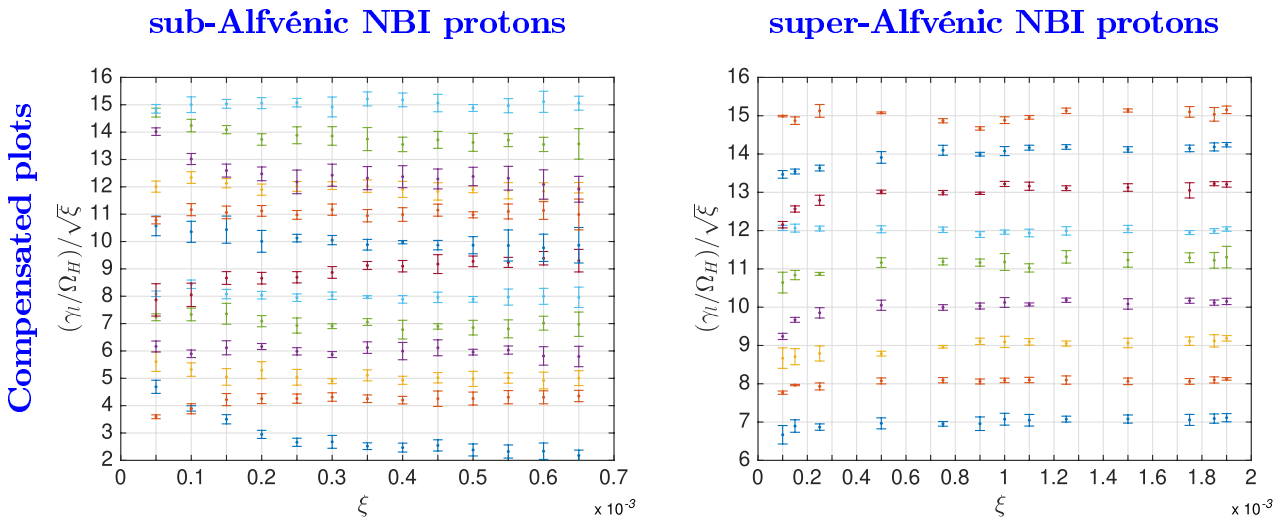

Figure 10. Dependence of early phase growth rates γ_ℓ in simulations at an angle of 89.5° with different NBI ion concentration ξ, obtained accross multiple cyclotron harmonics ℓ. Left and right panels correspond to LHD plasmas 79126 and 79003 respectively. Here $\gamma_\ell = \gamma_\ell(\xi)$ is the growth rate inferred from the simulations for mode number ℓ, and depends on the relative NBI density ξ at the ICE location. The translated compensated plots represent the quantity $(\gamma_\ell/\Omega_\mathrm{H})/\sqrt{\xi}$ versus ξ, with γ_ℓ inferred from simulations. If the simulation outputs match the linear theory of the MCI, we expect $\gamma_\ell/\Omega_\mathrm{H} = \alpha_\ell\sqrt{\xi}$ as in equation (9). In this case, it follows that $(\gamma_\ell/\Omega_\mathrm{H})/\sqrt{\xi} = \alpha_\ell$, a quantity that does not depend on ξ, but on the mode value ℓ only. This outcome is reflected by the sequence of horizontal lines in the compensated plots. The values of ξ span one order of magnitude, between 10^{-4} and 10^{-3}. Together, these graphs show that, within modest error bars, $\gamma_\ell \propto \sqrt{\xi}$.

the time domain. Once $B_z(k_{\ell\Omega_\mathrm{H}}, t)$ is calculated, we identify the interval $[t_0, t_1]$ over which the initial exponential growth phase takes place in our simulations. We find the duration of this initial exponential growth phase in the simulations to be $\approx 1.0\tau_\mathrm{H}$ for the fastest-growing modes, while the slowest-growing ones unfold over $\approx 20\tau_\mathrm{H}$. We perform multiple fits of $B_z(k_{\ell\Omega_\mathrm{H}}, t)$ between $[t_{1/2} - n\Delta t, t_{1/2} + n\Delta t]$ where: $t_{1/2}$ is at the centre of $[t_0, t_1]$, which are the start and end times of the initial exponential growth; $\Delta t \approx 0.001\tau_\mathrm{H}$; and n varies between 1 and n_max, such that $[t_{1/2} - n_\mathrm{max}\Delta t, t_{1/2} + n_\mathrm{max}\Delta t]$ is the smallest interval to contain $[t_0, t_1]$. This yields a family of n growth rates $\gamma_{\ell,n}, 1 \leqslant n \leqslant n_\mathrm{max}$ for a given mode at $\omega = \ell\Omega_\mathrm{H}$. We take the mean of the individual best fits as the growth rate value $\gamma_\ell = \bar{\gamma}_{\ell,n}$, and define the associated error $\Delta\gamma_\ell = \sigma(\gamma_{\ell,n})$, where the bar and sigma respectively represent the average and the standard deviation. The average and variance are taken between $n_\mathrm{min} \leqslant n \leqslant n_\mathrm{max}$, where n_min satisfies $n_\mathrm{min}\Delta t \geqslant 0.5\tau_\mathrm{H}/\ell$. That is, computation of the average starts from Δt corresponding to half an oscillation of the unstable ℓth mode. This enables us to use the same value of Δt for each cyclotron harmonic ℓ.

The procedure described above enables us to calculate growth rates denoted γ_ℓ for the ℓth harmonic during the early phase of simulations. These are next compared with the scaling of the analytical expressions for the corresponding growth rate $\gamma_\mathrm{lin}(\ell)$ of the MCI, notably equation (36) of [34] which reads:

$$\frac{\gamma_\mathrm{lin}(\ell)}{\Omega_\mathrm{H}} = \frac{1}{\sqrt{2}}\frac{V_\mathrm{A}}{v_\mathrm{NBI}}\frac{\omega_{p,\mathrm{NBI}}}{\omega_\mathrm{pi}}\chi_0 = \frac{1}{\sqrt{2}}\frac{V_\mathrm{A}}{v_\mathrm{NBI}}\sqrt{\frac{n_\mathrm{NBI}}{n_e}}\chi_0. \quad (7)$$

Here $\omega_{p,\mathrm{NBI}}$ and ω_pi are the plasma frequencies of the NBI protons and of the bulk protons respectively, and v_NBI is again the initial velocity of NBI protons. We define

$$\chi_0^2 = \Pi_{x,x} - \frac{2i\omega\Omega_\mathrm{H}}{V_\mathrm{A}^2k^2}\Pi_{x,y} + \frac{\Omega_\mathrm{H}^2}{V_\mathrm{A}^2k^2}\Pi_{y,y} \quad (8)$$

where $\Pi_{x,x}$, $\Pi_{x,y}$ and $\Pi_{y,y}$ are the functions of $z_\mathrm{NBI} = kv_\mathrm{NBI}/\Omega_\mathrm{H}$ as given in the appendix of [34]. Near resonance, $\omega_0 = V_\mathrm{A}k = \ell\Omega_\mathrm{H}$ and $z_\mathrm{NBI} = \ell v_\mathrm{NBI}/V_\mathrm{A}$. For a given mode ℓ, if all parameters are kept fixed except for the NBI proton density $\xi = n_\mathrm{NBI}/n_e$, equation (7) yields the scaling

$$\frac{\gamma_\mathrm{lin}(\ell)}{\Omega_\mathrm{H}} = \alpha_\ell\sqrt{\xi} \quad (9)$$

as in figure 10, where

$$\alpha_\ell \equiv \frac{1}{\sqrt{2}}\frac{V_\mathrm{A}}{v_\mathrm{NBI}}\chi_0 \quad (10)$$

which depends on ℓ solely. As stated above, the function χ_0 depends on the dimensionless parameter $v_\mathrm{NBI}/V_\mathrm{A}$ as well as on mode number ℓ. We have evaluated χ_0 in the super-Alfvénic and sub-Alfvénic cases for cyclotron harmonics between 5 and 15, and obtained roughly constant results of 0.35 and 0.15 respectively. Taking their ratios across these mode numbers range therefore yields a constant value of approximately 2.5, and translates into ratios of α_ℓ of approximately 2.05. Equation 36 of [34] hence predicts higher growth in the super-Alfvénic regime at constant beam density. The values α_ℓ are close to 0.30 and to 0.16 in the super- and sub-Alfvénic regimes respectively. This factor of 2 between these two regimes from analytical linear theory differs from the simulations. A possible explanation rests on the fact that analytical linear growth rates in the 1990s literature were calculated on the basis of a first order expansion about the cold plasma linear dispersion relation $\omega = kV_\mathrm{A}$. By contrast, in our present first principles computations, the real frequency of the

excited modes is determined by the self-consistent Maxwell–Lorentz dynamics, and is found to deviate progressively from the linear expression at increasingly high frequencies. Hence the location in (ω, k)-space of the dominant MCI drive differs increasingly from the location assumed in linear theory, at increasingly high cyclotron harmonics. This is visible in figure 4; the extent of any deviation of early-time growth rates from linear theory can only be established reliably, for a given scenario, by running the code. Our code outputs yield continuity between early-time growth rates as one transitions across the boundary between sub-Alfvénic and super-Alfvénic regimes for the particular parameter sets considered, whereas linear analytical theory yields a difference by a factor of order two.

We test the hypothesis that $\gamma_\ell \simeq \gamma_{\text{lin}}(\ell)$ by running multiple simulations for different values of the beam proton density ratio ξ, with all other parameters kept fixed. The computed growth rates at early times γ_ℓ for a given mode ℓ, obtained by means of $B_\xi(k_{\ell\Omega_H}, t)$ as appeared in figure 8, are then plotted against $\sqrt{\xi}$, in line with the analytical scaling of $\gamma_{\text{lin}}(\ell)$ [5, 34] in equation (9) as shown in figure 9. The values of the growth rates obtained in our PIC hybrid calculations are similar between the sub- and super-Alfvénic regimes for comparable NBI proton densities; and the numerically computed values of α_ℓ are about five for harmonic numbers between 5–15 in both regimes.

More generally, figure 9 shows congruence between the early phase of collective relaxation of the NBI ion population in our first principles PIC-hybrid simulations, and the analytical theory of the linear stage of the MCI. It tends to confirm that the resulting ICE spectra can be understood in terms of the MCI, which our simulations extend into the analytically inaccessible nonlinear regime, for both sub-Alfvénic and super-Alfvénic NBI proton populations.

The procedure is now applied accross multiple harmonic modes with the results shown figure 10.

As in figure 9, in figure 10 we plot the dependence of the growth rate γ_ℓ of the fields, calculated at early times in multiple simulations, on NBI concentration ξ in each simulation. The computations are performed for parameters corresponding to LHD plasmas 79126 and 79003. In both scenarios, the propagation angle between $\mathbf{B}_0$ and $\mathbf{k}$ is 89.5°. The pair of panels in figure 10 instead reformulates equation (9) as

$$(\gamma_{\text{lin}}(\ell)/\Omega_H)/\sqrt{\xi} = \alpha_\ell. \tag{11}$$

This implies that for a fixed mode number ℓ, the quantity $(\gamma_{\text{lin}}(\ell)/\Omega_H)/\sqrt{\xi}$ is independent of ξ and equals a constant that depends on ℓ solely. We translate that constant such that it equals to $\alpha'_\ell = \ell$. Figure 10 strongly suggests that in general $\gamma_\ell \sim \xi^{1/2}$ in our simulations, across an extended range of modes. This dependence is the same as for growth rates from linear analysis of the MCI [34], and from previous simulations e.g. figure 3 of [39]. Additional linear and cubic root scaling tests have been performed, and F-test statistics [61] applied with a 99% significance further confirm the square root scaling.

We have also investigated, through PIC-hybrid simulations, the collective relaxation of NBI proton populations that have artificially enhanced sub- and super-Alfvénic characteristics under the LHD plasma conditions already considered. We have run multiple simulations of a sub-Alfvénic fast proton population of 25 keV, for which $v_{\text{NBI}}/V_A = 0.7$ under LHD plasma 79126 conditions, as well as simulations with a 56 keV super-Alfvénic fast proton beam, for which $v_{\text{NBI}}/V_A = 1.4$ under LHD 79003 plasma edge conditions. The same conclusions are obtained.

7. Conclusions

Several advances are reported in this paper. First, we have presented the first 1D3V PIC-hybrid simulations of ICE where the minority energetic ion population arises from NBI, hence with kinetic energy more than an order of magnitude lower than in previous simulations [25, 30–32, 39] relating to super-Alfvénic fusion-born ions in JET. Second, first principles kinetic simulations of ICE and MCI physics in the sub-Alfvénic regime for energetic ions have not previously been carried out, with one exception. This exception is the set of multiple PIC simulations [31, 32] of ICE driven by fusion-born protons under rapidly evolving edge plasma conditions in KSTAR where, for local electron densities below $n_e \sim 1.05 \times 10^{19}$ m^{-3}, corresponding to the lower panels of figure 4 of [31], the perpendicular velocity of the protons is sub-Alfvénic. We have found that, in the LHD-relevant context, the transition between sub-Alfvénic and super-Alfvénic ICE phenomenology is extremely smooth, both in observations and simulations.

A third novel aspect of this paper is that it is the first to report first principles kinetic ICE simulations with wavevectors inclined more than one degree from perpendicular to the magnetic field direction. While more challenging computationally, this leads to better congruence of simulation outputs with the observed ICE spectra, as in figure 6, and is helpful in a context where antenna sensitivity may not be known in detail as a function of $k_\parallel$ in the relevant range. Fourth, we have carried out the first study of early-time growth rates inferred from simulations that span sub-Alfvénic and super-Alfvénic energetic ion regimes. Of particular interest is how these growth rates depend on energetic ion concentration $\xi = n_{\text{NBI}}/n_e$; figure 10 establishes a square root scaling with ξ, in line with prediction from the corresponding linear analytical MCI theory [34]. For simulations relevant to the super-Alfvénic regime, this scaling was established in [39].

In summary, the measured ion cyclotron emission (ICE) spectra (figure 2) from LHD hydrogen plasmas with both sub-Alfvénic and super-Alfvénic perpendicular proton NBI have been successfully simulated (figure 6) using a first principles approach. Direct numerical simulation of kinetic ions (bulk protons and minority energetic NBI protons) and fluid electrons using a 1D3V PIC-hybrid code captures the self-consistent Maxwell–Lorentz dynamics of the plasma and fields. It is found from the Fourier transforms and time evolution

of the energy and field components in the PIC-hybrid code outputs that the dominant physical process in our first principles Maxwell–Lorentz computations is the magnetoacoustic cyclotron instability (MCI). The many correlations between our code outputs and the measured ICE spectra suggest that an emission mechanism, which corresponds essentially to the nonlinear MCI, is responsible for the main features of ICE in these LHD stellarator plasmas. In the context of the extensive prior research on the role of the MCI in ICE from tokamak plasmas, this outcome suggests a significant degree of commonality across tokamak and stellarator ICE physics. This appears to be a consequence of the strongly spatially localised character of ICE physics, and implies that overall magnetic geometry plays a relatively minor role. The spontaneously excited electric and magnetic fields in our simulations, which are carried out in local slab geometry, correspond to the fast Alfvén wave. This work helps establish a baseline for future energetic particle experiments in LHD, where magnetic geometry and toroidal eigenfunctions [62] may play a larger role. ICE links beam ion physics in LHD to fusion-born ion physics in tokamaks, and has significant diagnostic potential [20].

Acknowledgments

This work has been carried out within the framework of the EUROfusion Consortium and has received funding from the Euratom research and training programme 2014–2018 and 2019–2020 under Grant Agreement No. 633053. The work received support from the RCUK Energy Programme [Grant No. EP/P012450/1 and EP/I501045], NIFS budget NIFS15KLPF045 and ULHH029 and from NRF Korea Grant No. 2014M1A7A1A03029881. The views and opinions expressed herein do not necessarily reflect those of the European Commission. ROD acknowledges the hospitality of Kyushu University. BCGR acknowledges helpful discussion with Dr Carbajal-Gomez.

ORCID iDs

S.C. Chapman https://orcid.org/0000-0003-0053-1584
G.S. Yun https://orcid.org/0000-0002-1880-5865

References

[1] Dendy R.O. and McClements K. 2015 Ion cyclotron emission from fusion-born ions in large tokamak plasmas: a brief review from JET and TFTR to ITER *Plasma Phys. Control. Fusion* **57** 044002
[2] Gorelenkov N.N. 2016 Ion cyclotron emission studies: retrospects and prospects *Plasma Phys. Rep.* **42** 430–9
[3] Equipe T. 1978 High-power neutral injection and ion power balance in TFR *Nucl. Fusion* **18** 1271
[4] Bhadra D., Chiu S., Buchenauer D. and Hwang D. 1986 Electromagnetic emission from a neutral-beam-injected plasma *Nucl. Fusion* **26** 201
[5] Cottrell G. and Dendy R.O. 1988 Superthermal radiation from fusion products in JET *Phys. Rev. Lett.* **60** 33–6
[6] Cauffman S. and Majeski R. 1995 Ion cyclotron emission on the tokamak fusion fest reactor *Rev. Sci. Instrum.* **66** 817–9
[7] Kimura H. *et al* 1998 Alfvén eigenmode and energetic particle research in JT-60U *Nucl. Fusion* **38** 1303
[8] D'Inca M. García Muñoz R., Tardini G., Noterdaeme J.M. and The ASDEX Upgrade Team 2011 Characteristics of ion cyclotron emission on ASDEX upgrade *38th EPS Conf. on Plasma Physics (Strasbourg, 27 June–1 July 2011)* (http://ocs.ciemat.es/EPS2011PAP/pdf/P1.053.pdf)
[9] Thatipamula S.G., Yun G., Leem J., Park H.K., Kim K., Akiyama T. and Lee S. 2016 Dynamic spectra of radio frequency bursts associated with edge-localized modes *Plasma Phys. Control. Fusion* **58** 065003
[10] Heidbrink W. *et al* 2011 Characterization of off-axis fishbones *Plasma Phys. Control. Fusion* **53** 085028
[11] Saito K. *et al* 2009 Measurement of ion cyclotron emissions by use of ICRF heating antennas in LHD *Fusion Eng. Des.* **84** 1676–9
[12] Saito K. *et al* (LHD Experiment Group) 2013 Measurement of ion cyclotron emissions by using high frequency magnetic probes in the LHD *Plasma Sci. Technol.* **15**
[13] Shalashov A. *et al* 2003 NBI-driven ion cyclotron instabilities at the W7-AS stellarator *Plasma Phys. Control. Fusion* **45** 395
[14] Cottrell G., Bhatnagar V., Da Costa O., Dendy R., Jacquinot J., McClements K., McCune D., Nave M., Smeulders P. and Start D. 1993 Ion cyclotron emission measurements during JET deuterium–tritium experiments *Nucl. Fusion* **33** 1365
[15] Cauffman S., Majeski R., McClements K.G. and Dendy R.O. 1995 Alfvenic behaviour of alpha particle driven ion cyclotron emission in TFTR *Nucl. Fusion* **35** 1597–602
[16] Dendy R., McClements K., Lashmore-Davies C., Cottrell G., Majeski R. and Cauffman S. 1995 Ion cyclotron emission due to collective instability of fusion products and beam ions in TFTR and JET *Nucl. Fusion* **35** 1733
[17] McClements K., Hunt C., Dendy R. and Cottrell G. 1999 Ion cyclotron emission from JET DT plasmas *Phys. Rev. Lett.* **82** 2099–102
[18] Thome K., Pace D., Pinsker R., Meneghini O., del Castillo C. and Zhu Y. 2018 Radio frequency measurements of energetic-particle-driven emission using the ion cyclotron emission diagnostic on the DIII-D tokamak *Rev. Sci. Instrum.* **89** 10I102
[19] Ochoukov R. *et al* 2018 Observations of core ion cyclotron emission on ASDEX Upgrade tokamak *Rev. Sci. Instrum.* **89** 10J101
[20] McClements K., D'Inca R., Dendy R.O., Carbajal L., Chapman S., Cook J., Harvey R., Heidbrink W. and Pinches S. 2015 Fast particle-driven ion cyclotron emission (ICE) in tokamak plasmas and the case for an ICE diagnostic in ITER *Nucl. Fusion* **55** 043013
[21] Osakabe M. *et al* 2006 Experimental observations of enhanced radial transport of energetic particles with Alfvén eigenmode on the LHD *Nucl. Fusion* **46** S911
[22] Toi K., Ogawa K., Isobe M., Osakabe M., Spong D.A. and Todo Y. 2011 Energetic-ion-driven global instabilities in stellarator/helical plasmas and comparison with tokamak plasmas *Plasma Phys. Control. Fusion* **53** 024008
[23] Sharapov S. *et al* 2013 Energetic particle instabilities in fusion plasmas *Nucl. Fusion* **53** 104022
[24] Todo Y., Van Zeeland M. and Heidbrink W. 2016 Fast ion profile stiffness due to the resonance overlap of multiple Alfvén eigenmodes *Nucl. Fusion* **56** 112008
[25] Carbajal L., Dendy R.O., Chapman S. and Cook J. 2014 Linear and nonlinear physics of the magnetoacoustic cyclotron instability of fusion born-ions in relation to ion cyclotron emission *Phys. Plasmas* **21** 012106

[26] Darwin C.G. 1920 The dynamical motions of charged particles *Lond. Edinburgh Dublin Phil. Mag. J. Sci.* **39** 537–51

[27] Arber T. *et al* 2015 Contemporary particle-in-cell approach to laser-plasma modelling *Plasma Phys. Control. Fusion* **57** 113001

[28] Cook J., Chapman S. and Dendy R. 2010 Electron current drive by fusion-product-excited lower hybrid drift instability *Phys. Rev. Lett.* **105** 255003

[29] Cook J., Dendy R.O. and Chapman S. 2013 Particle-in-cell simulations of the magnetoacoustic cyclotron instability of fusion-born alpha particles in tokamak plasmas *Plasma Phys. Control. Fusion* **55** 065003

[30] Cook J., Dendy R. and Chapman S. 2017 Stimulated emission of fast Alfvén waves within magnetically confined fusion plasmas *Phys. Rev. Lett.* **118** 185001

[31] Chapman B., Dendy R., McClements K., Chapman S., Yun G., Thatipamula S. and Kim M. 2017 Sub-microsecond temporal evolution of edge density during edge localized modes in KSTAR tokamak plasmas inferred from ion cyclotron emission *Nucl. Fusion* **57** 124004

[32] Chapman B., Dendy R.O., Chapman S.C., McClements K.G., Yun G.S., Thatipamula S.G. and Kim M. 2018 Nonlinear wave interactions generate high-harmonic cyclotron emission from fusion-born protons during a KSTAR ELM crash *Nucl. Fusion* **58** 096027

[33] Belikov V. and Kolesnichenko Y.I. 1976 *Sov. Phys. Tech. Phys.* **20** 1146

[34] Dendy R., Lashmore Davies C.N. and Kam K. 1992 A possible excitation mechanism for observed superthermal ion cyclotron emission from tokamak plasmas *Phys. Fluids* B **4** 3996–4006

[35] Dendy R.O., Lashmore Davies C. and Kam K.F. 1993 The magnetoacoustic cyclotron instability of an extended shell distribution of energetic ions *Phys. Fluids* B **5** 1937–44

[36] Dendy R., Lashmore-Davies C., McClements K. and Cottrell G. 1994 The excitation of obliquely propagating fast Alfvén waves at fusion ion cyclotron harmonics *Phys. Plasmas* **1** 1918–28

[37] Dendy R., McClements K., Lashmore-Davies C., Majeski R. and Cauffman S. 1994 A mechanism for beam-driven excitation of ion cyclotron harmonic waves in the Tokamak Fusion Test Reactor *Phys. Plasmas* **1** 3407–13

[38] McClements K.G., Dendy R.O., Lashmore Davies C., Cottrell G.A., Cauffman S. and Majeski R. 1995 Interpretation of ion cyclotron emission from subAlfvénic fusion products in the tokamak fusion test reactor *Phys. Plasmas* **3** 543–53

[39] Carbajal L., Dendy R., Chapman S. and Cook J. 2017 Quantifying fusion born ion populations in magnetically confined plasmas using ion cyclotron emission *Phys. Rev. Lett.* **118** 105001

[40] McClements K. and Dendy R. 1993 Ion cyclotron harmonic wave generation by ring protons in space plasmas *J. Geophys. Res.: Space Phys.* **98** 11689–700

[41] Dendy R.O. 1990 *Plasma Dynamics* (Oxford: Clarendon)

[42] Appel L.C. *et al* (MAST Team) 2008 Compressional Alfvén eigenmodes on mast *Plasma Phys. Control. Fusion* **50** 115011

[43] Fredrickson E. *et al* 2013 Non-linear modulation of short wavelength compressional Alfvén eigenmodes *Phys. Plasmas* **20** 042112

[44] Sharapov S., Lilley M., Akers R., Ayed N.B., Cecconello M., Cook J., Cunningham G., Verwichte E. and MAST Team 2014 Bi-directional Alfvén cyclotron instabilities in the mega-amp spherical tokamak *Phys. Plasmas* **21** 082501

[45] Crocker N., Kubota S., Peebles W., Rhodes T., Fredrickson E., Belova E., Diallo A., LeBlanc B. and Sabbagh S. 2017 Density perturbation mode structure of high frequency compressional and global Alfvén eigenmodes in the national spherical torus experiment using a novel reflectometer analysis technique *Nucl. Fusion* **58** 016051

[46] Belova E., Gorelenkov N., Fredrickson E., Tritz K. and Crocker N. 2015 Coupling of neutral-beam-driven compressional Alfvén eigenmodes to kinetic Alfvén waves in NSTX tokamak and energy channeling *Phys. Rev. Lett.* **115** 015001

[47] Büchner J., Dum C. and Scholer M. 2003 *Space Plasma Simulation* vol 615 (Berlin: Springer)

[48] JET Team *et al* 1992 Fusion energy production from a deuterium–tritium plasma in the JET tokamak *Nucl. Fusion* **32** 187

[49] Fülöp T., Kolesnichenko Y.I., Lisak M. and Anderson D. 1997 Origin of superthermal ion cyclotron emission in tokamaks *Nucl. Fusion* **37** 1281–93

[50] Birdsall C.K. and Langdon A.B. 2004 *Plasma Physics via Computer Simulation* (Boca Raton, FL: CRC Press)

[51] Hockney R.W. and Eastwood J.W. 1988 *Computer Simulation using Particles* (Boca Raton, FL: CRC Press)

[52] Winske D. and Omidi N. 1991 Hybrid codes: Methods and applications *Technical Report* Los Alamos National Lab., NM, USA

[53] Fisch N.J. 2016 Pushing particles with waves: current drive and α-channeling *Plasma Fusion Res.* **11** 2101010

[54] Bustos A., Castejón F., Osakabe M., Fernández L., Martin-Mayor V., Guasp J. and Fontdecaba J. 2011 Kinetic simulations of fast ions in stellarators *Nucl. Fusion* **51** 083040

[55] Gingell P.W., Chapman S.C., Dendy R.O. and Brady C.S. 2012 Transport and evolution of ion gyro-scale plasma blobs in perpendicular magnetic fields *Plasma Phys. Control. Fusion* **54** 065005

[56] Winske D., Yin L., Omidi N., Karimabadi H. and Quest K. 2003 *Hybrid Simulation Codes: Past, Present and Future—A Tutorial* (Berlin: Springer) pp 136–65

[57] Lee R., Chapman S. and Dendy R. 2004 Numerical simulations of local shock reformation and ion acceleration in supernova remnants *Astrophys. J.* **604** 187

[58] Sydora R. 1999 Low-noise electromagnetic and relativistic particle-in-cell plasma simulation models *J. Comput. Appl. Math.* **109** 243–59

[59] Murakami S., Nakajima N. and Okamoto M. 1995 Finite β effects on the ICRF and NBI heating in the large helical device *Fusion Technol.* **27** 256–9

[60] Stix T.H. 1975 Fast-wave heating of a two-component plasma *Nucl. Fusion* **15** 737

[61] Bendat J.S. and Piersol A.G. 2011 *Random Data: Analysis and Measurement Procedures* vol 729 (Hoboken, NJ: Wiley)

[62] Gorelenkov N. and Cheng C. 1995 Excitation of Alfvén cyclotron instability by charged fusion products in tokamaks *Phys. Plasmas* **2** 1961–71